

RESEARCH ARTICLE

Simultaneous assessment of both lung morphometry and gas exchange function within a single breath-hold by hyperpolarized ^{129}Xe MRI

Jianping Zhong^{1,2} | Huiting Zhang^{1,2} | Weiwei Ruan² | Junshuai Xie² | Haidong Li² | He Deng² | Yeqing Han² | Xianping Sun² | Chaohui Ye^{1,2} | Xin Zhou² ¹School of Physics, Huazhong University of Science and Technology, Wuhan, China²Key Laboratory of Magnetic Resonance in Biological Systems, State Key Laboratory of Magnetic Resonance and Atomic and Molecular Physics, National Center for Magnetic Resonance in Wuhan, Wuhan Institute of Physics and Mathematics, Chinese Academy of Sciences, Wuhan, China**Correspondence**

Xin Zhou, National Center for Magnetic Resonance in Wuhan, Wuhan Institute of Physics and Mathematics, Chinese Academy of Sciences, 30 West Xiaohongshan, Wuhan 430071, China.

Email: xinzhou@wipm.ac.cn

Funding information

National Natural Science Foundation of China, Grant/Award Number: 81227902 and 81625011; National Program for Support of Top-notch Young Professionals; Opening Project of Wuhan National High Magnetic Field Center, Grant/Award Number: 2015KF09

During the measurement of hyperpolarized ^{129}Xe magnetic resonance imaging (MRI), the diffusion-weighted imaging (DWI) technique provides valuable information for the assessment of lung morphometry at the alveolar level, whereas the chemical shift saturation recovery (CSSR) technique can evaluate the gas exchange function of the lungs. To date, the two techniques have only been performed during separate breaths. However, the request for multiple breaths increases the cost and scanning time, limiting clinical application. Moreover, acquisition during separate breath-holds will increase the measurement error, because of the inconsistent physiological status of the lungs. Here, we present a new method, referred to as diffusion-weighted chemical shift saturation recovery (DWCSSR), in order to perform both DWI and CSSR within a single breath-hold. Compared with sequential single-breath schemes (namely the 'CSSR + DWI' scheme and the 'DWI + CSSR' scheme), the DWCSSR scheme is able to significantly shorten the breath-hold time, as well as to obtain high signal-to-noise ratio (SNR) signals in both DWI and CSSR data. This scheme enables comprehensive information on lung morphometry and function to be obtained within a single breath-hold. *In vivo* experimental results demonstrate that DWCSSR has great potential for the evaluation and diagnosis of pulmonary diseases.

KEYWORDS

CSSR, DWCSSR, DWI, hyperpolarized, lung, xenon-129

1 | INTRODUCTION

Pulmonary function tests (PFTs), chest X-rays and computed tomography (CT) are the most widely used clinical techniques for pulmonary disease diagnosis. However, PFTs cannot visualize and quantify lung microstructural parameters, and chest X-rays and CT are limited by ionizing radiation. In contrast, hyperpolarized (HP) noble gases (^3He , ^{129}Xe) nuclear magnetic resonance (NMR) and magnetic resonance imaging (MRI) have been proven to be powerful non-invasive tools for the quantitative detection of both lung microstructure¹⁻³ and function.⁴⁻⁶ In comparison with ^3He , ^{129}Xe has higher natural abundance and lower cost. Recent studies have also shown improvement in ^{129}Xe spin polarization,⁷⁻⁹ allowing the images of ^{129}Xe to be of comparable quality to those of ^3He .¹⁰ Meanwhile, ^{129}Xe has good solubility in tissues and blood,¹¹ making the assessment of gas exchange possible. As a result of these properties, ^{129}Xe has become more attractive for *in vivo* functional studies of the lungs.

In HP ^{129}Xe studies, the gas exchange function of the lungs has commonly been assessed by direct dissolved ^{129}Xe imaging,^{12,13} xenon polarization transfer contrast (XTC)^{14,15} and chemical shift saturation recovery (CSSR)^{16,17} techniques. The direct dissolved ^{129}Xe imaging technique, imaging both the dissolved ^{129}Xe signals [i.e. ^{129}Xe dissolved in tissue and plasma (TP) and in red blood cells (RBCs)] and the gaseous ^{129}Xe signals

Abbreviations used: ADC, apparent diffusion coefficient; CAS, Chinese Academy of Sciences; COPD, chronic obstructive pulmonary disease; CSSR, chemical shift saturation recovery; CT, computed tomography; DKI, diffusional kurtosis imaging; DWCSSR, diffusion-weighted chemical shift saturation recovery; DWI, diffusion-weighted imaging; FID, free induction decay; Hct, blood hematocrit; HP, hyperpolarized; MOXE, model of xenon exchange; MRI, magnetic resonance imaging; NMR, nuclear magnetic resonance; PFTs, pulmonary function tests; RBC, red blood cell; RF, radiofrequency; SAR, specific absorption ratio; SNR, signal-to-noise ratio; SVR, surface-to-volume ratio; TP, tissue and plasma; WIPM, Wuhan Institute of Physics and Mathematics; XTC, xenon polarization transfer contrast

simultaneously, provides visual dissolved ^{129}Xe maps directly. The XTC technique, measuring the decrease in the gaseous ^{129}Xe signal after saturation of dissolved ^{129}Xe signals, generates the dissolved ^{129}Xe maps indirectly. The CSSR technique, measuring the time-dependent build-up of dissolved ^{129}Xe signals after saturation, observes the average gas exchange functions of the entire lung. Among these techniques, CSSR has a unique advantage in that it can obtain dynamic information on the dissolved ^{129}Xe signals in both TP and RBCs. Meanwhile, combined with gas exchange models, such as the Patz model,¹⁸ the Månsson model¹⁶ and the model of xenon exchange (MOXE),¹⁹ the gas exchange function parameters, including the capillary transit time (t_c), septal thickness (d), surface-to-volume ratio (SVR), etc., can be extracted from CSSR data. Therefore, CSSR has been widely used in both animal and human studies for the detection of pulmonary diseases, such as chronic obstructive pulmonary disease (COPD),^{18,20} idiopathic pulmonary fibrosis,⁴ interstitial lung disease¹⁸ and radiation-induced lung injury.^{21,22}

On the other hand, diffusion information on ^{129}Xe gas in lung airspaces, which is commonly observed by the diffusion-weighted imaging (DWI) technique, could provide valuable information on the lung microstructure at the alveolar level. To date, ^{129}Xe DWI has been widely applied for the detection of pulmonary diseases, such as COPD^{23,24} and emphysema,^{25,26} in both animal and human studies. DWI with two b values (commonly referred to as zero b value and non-zero b value)^{25,27} has been proposed to extract the apparent diffusion coefficient (ADC) of ^{129}Xe gas, which is an index for the assessment of alveolar enlargement in subjects with COPD. The ^{129}Xe lung morphometry method, developed by Sukstanskii and Yablonskiy et al.,²⁸ which is based on DWI with multiple b values, could further visualize and quantify the lung morphological parameters, such as the external radius (R) and internal radius (r) of the pulmonary acinus, mean linear intercept (L_m), etc.

Lung can be viewed as consisting of two major structures: the acinar airways (ducts and sacs) and blood capillary circuits. The microstructure of the former can be assessed by the ^{129}Xe DWI technique, whereas the microstructure of the latter, as well as the gas exchange function, can be explored by the CSSR technique. Thus, a combination of DWI and CSSR can provide comprehensive information with regard to both the lung microstructure and gas exchange function, despite the fact that CSSR measures the average parameters of the entire lung, whereas DWI measures the regional diffusivity. However, to our knowledge, these two techniques have only been performed together during different breath-holds,²² which limits their practicability and efficiency. Acquisition during separate breath-holds also increases the measurement error and cost. Sequential schemes (i.e. performing DWI after CSSR, or CSSR after DWI) are feasible for performing both CSSR and DWI within a single breath-hold, although they have not been proposed previously. However, the breath-hold times of sequential single-breath schemes would be quite long. In addition, because of the longitudinal relaxation and radiofrequency (RF) excitations of ^{129}Xe gas, the DWI data during the sequential 'CSSR + DWI' scheme, as well as the CSSR data during the sequential 'DWI + CSSR' scheme, would be limited by low signal-to-noise ratio (SNR). However, the post-processing of both DWI and CSSR data requires a high SNR.

In this study, we propose a new method to accelerate the performance of both CSSR and DWI within a single breath-hold. The so-called diffusion-weighted chemical shift saturation recovery (DWCSSR) method can be performed within a short breath-hold, and is able to achieve high SNR signals for both CSSR and DWI measurements. We compared DWCSSR with the two sequential single-breath schemes (i.e. 'CSSR + DWI' scheme and 'DWI + CSSR' scheme) during *in vivo* experiments. Both the gas exchange function and microstructure of the lungs can be explored by DWCSSR during a single scan.

2 | THEORY

2.1 | Pulse sequence

Traditional single-breath CSSR and DWI sequences are shown in Figure 1a and 1b, respectively. In CSSR, both RF pulses α_1 and α_2 are used to excite the dissolved ^{129}Xe signals. α_1 is intended to yield a minimal on-resonance excitation of gaseous ^{129}Xe , whereas α_2 is applied to yield a considerable gaseous ^{129}Xe signal for normalization. The exchange times (τ) are varied from 0 to 900 ms,^{19,20} whereas TR of DWI is less than

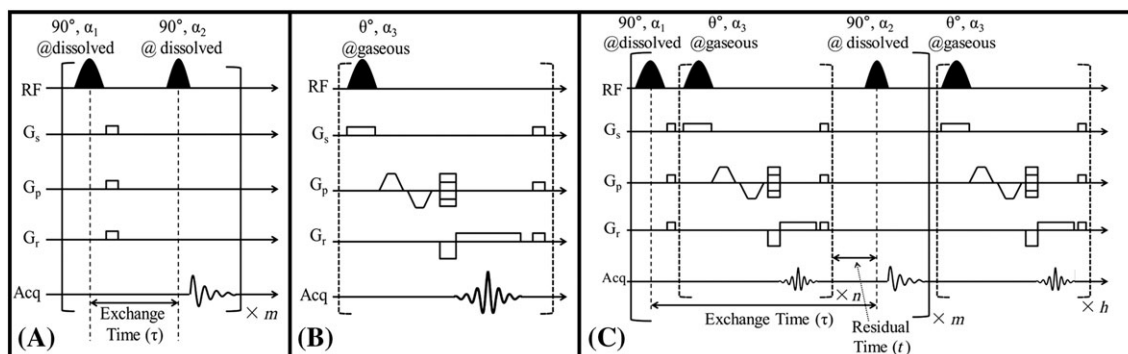


FIGURE 1 Pulse sequences of traditional chemical shift saturation recovery (CSSR) A, traditional diffusion-weighted imaging (DWI) B, and diffusion-weighted chemical shift saturation recovery (DWCSSR) C. The essence of DWCSSR is the performance of DWI repetitions during the exchange time (τ) of CSSR

20 ms in most cases. Therefore, DWI repetitions can be performed during the exchange times of CSSR, in order to accelerate the acquisitions of both CSSR and DWI. This acquisition scheme is referred to as DWCSSR, as shown in Figure 1c. In DWCSSR, exchange times are mostly utilized to perform DWI, whereas only a small residual time (t) remains. If the total DWI repetitions cannot be finished within the entire exchange times, the remaining DWI repetitions (denoted as h) are performed after the entire m repetitions of CSSR.

Parameters n , t and h in Figure 1c are estimated according to the equations below. Assuming that TR of DWI (i.e. minimum duration between two sequential excitations of α_3) is TR_{DW} , the entire repetition number of CSSR is m and the varied exchange times of CSSR are τ_k , the maximum number (f_k) for performing DWI within each exchange time τ_k is:

$$f_k = Q \cdot \left\lfloor \frac{\tau_k - \lambda}{Q \cdot TR_{DW}} \right\rfloor, \quad \tau_k \geq \lambda, \quad k = 1, 2, \dots, m \quad (1)$$

where λ is the total duration of both the RF pulses and spoiled gradients within the exchange times, operator $\lfloor \cdot \rfloor$ means getting the maximum non-negative integer which is smaller than that inside the brackets, and Q is a factor referring to the number of slices (N_S) of DWI. Q is equal to optional positive integer in the non-slice selection DWI case. In the multi-slice DWI case, Q should be an integral ratio of N_S , in order to keep the same CSSR exchange conditions for different slices. Assuming that the entire repetition number of DWI is ε and

$$\varepsilon = a \cdot N_y \cdot N_S \cdot N_b \quad (2)$$

where a is the under-sampling ratio, N_y is the size of the DW images along the phase-encoding direction and N_b is the number of b values. Combined with Equations 1 and 2, the actual number n_k for performing DWI within the exchange time τ_k is:

$$n_k = \begin{cases} f_k, & \sum_{i=1}^k f_i \leq \varepsilon \\ \varepsilon - \sum_{i=1}^{k-1} f_i, & \sum_{i=1}^k f_i > \varepsilon \text{ \& } \sum_{i=1}^k f_i - f_k < \varepsilon \\ 0, & \text{else} \end{cases}, \quad k = 1, 2, \dots, m \quad (3)$$

The residual time (t) within each exchange time τ_k is:

$$t_k = \tau_k - \lambda - n_k \cdot TR_{DW}, \quad \tau_k \geq \lambda, \quad k = 1, 2, \dots, m \quad (4)$$

The number (h) of the remaining DWI repetitions is:

$$h = \begin{cases} \varepsilon - \sum_{k=1}^m f_k, & \sum_{k=1}^m f_k \leq \varepsilon \\ 0, & \text{else} \end{cases}, \quad k = 1, 2, \dots, m \quad (5)$$

In general, if we know the exchange time (τ) of CSSR, the entire repetition number (m) of CSSR, the TR of DWI (TR_{DW}) and the entire repetition number (ε) of DWI, the parameters n , t and h can be obtained from Equations 3–5.

2.2 | Effects on CSSR data during DWCSSR

In traditional single-breath CSSR, the gaseous ^{129}Xe longitudinal magnetization (denoted as S_{gas}) is reduced over time as a result of both T_1 relaxation and gas exchange of gaseous ^{129}Xe .¹⁶ In DWCSSR, the α_3 excitations contribute to extra reductions of S_{gas} . The S_{gas} after a certain exchange time τ_k can be simply expressed as:

$$S_{\text{gas}}(\tau_k) \propto S_0 \cdot \exp\left(-\frac{\tau_k}{T_1}\right) \cdot [1 - F(\tau_k)] \cdot (\cos \alpha_3)^{\frac{n_k}{N_S}} \quad (6)$$

where S_0 is the gaseous ^{129}Xe magnetization at the beginning point of τ_k ; $\exp\left(-\frac{\tau_k}{T_1}\right)$, $[1 - F(\tau_k)]$ and $(\cos \alpha_3)^{\frac{n_k}{N_S}}$ are related to T_1 relaxation, the gas exchange fraction $F(\tau_k)$ and the extra α_3 excitations, respectively. During short exchange times (i.e. $\tau_k < Q \cdot TR_{DW}$), the number of α_3 excitations is zero (i.e. $n_k = 0$), so that S_{gas} in DWCSSR is the same as that in traditional CSSR. During medium exchange times (i.e. τ_k slightly larger than $Q \cdot TR_{DW}$), the loss of S_{gas} in DWCSSR is not significant because of the small n_k values. However, during long exchange times (i.e. $\tau_k \gg Q \cdot TR_{DW}$), the loss of S_{gas} will be more significant because of the relatively larger n_k values. However, according to previous HP ^{129}Xe DWI studies,^{23,24} the flip angle α_3 is commonly around a small value of 5° , so as to reduce the bias of initial gaseous ^{129}Xe magnetizations among different b values. In addition, the number of whole lung α_3 excitations $\left(\frac{n_k}{N_S}\right)$ can be reduced by increasing N_S . In a simulation case of $TR_{DW} = 13$ ms, $\alpha_3 = 5.5^\circ$, $T_1 = 15$ s and $\tau_k = 900$ ms, as shown in Figure 2a, the decay of S_{gas} is significantly slowed down as N_S increases. Moreover, during the case of $N_S = 5$, the total number of whole lung α_3 excitations is only 18, and the extra loss of gaseous ^{129}Xe magnetization as a result of α_3 excitations is only 8%. Even during the same case of traditional CSSR, the loss of S_{gas} is close to 8%. Therefore, in theory, a small flip angle α_3 and a small number of whole lung α_3 excitations will not yield significant loss of S_{gas} in multi-slice DWCSSR. Moreover, according to Patz et al.,¹⁸ the dissolved ^{129}Xe build-up function is an intensive quantity, depending only on the ratio of dissolved ^{129}Xe magnetization to gaseous ^{129}Xe magnetization. Thus, by

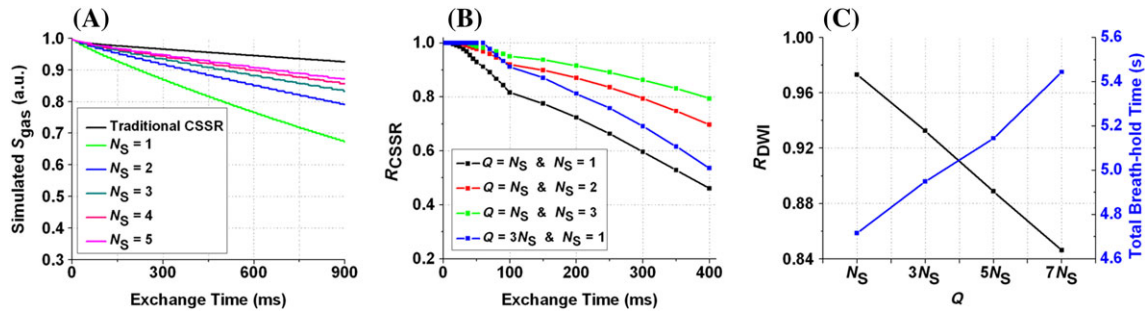


FIGURE 2 Simulation results of diffusion-weighted chemical shift saturation recovery (DWCSSR). A, gaseous ^{129}Xe magnetization S_{gas} during different time points within a 900 ms exchange time, which is simulated based on equation 6. The decay of S_{gas} in DWCSSR is quicker than that in traditional chemical shift saturation recovery (CSSR) because of the measurement of DWI during the exchange times. It should be noted that the increase in the number of slices (N_S) can significantly slow down the decay of S_{gas} . B, simulated R_{CSSR} (ratios of SNR_{CSSR} in DWCSSR to SNR_{CSSR} in traditional CSSR) values based on equation 7. It should be noted that the R_{CSSR} values increase with increasing N_S and Q . C, simulated R_{DWI} (black) and total breath-hold times (blue). It should be noted that R_{DWI} decreases with increasing Q . SNR, signal-to-noise ratio

calculating the ratio of dissolved ^{129}Xe magnetization to gaseous ^{129}Xe magnetization, the extra loss of magnetization during DWCSSR can be compensated for.

2.3 | SNR effects of DWCSSR

In single-breath DWCSSR, SNR of CSSR data during the last few exchange times will be reduced by the extra α_3 excitations. Compared with traditional CSSR, the extra reduction of S_{gas} during DWCSSR is referred to as $(\cos \alpha_3)^{\frac{n_k}{N_S}}$, according to Equation 6. Thus, the ratios of SNR_{CSSR} (SNR of CSSR) in DWCSSR to those in traditional CSSR during each exchange time τ_k will be:

$$R_{\text{CSSR}}(\tau_k) = (\cos \alpha_3)^{\frac{\sum_{i=1}^k n_i}{N_S}}, k = 1, 2, \dots, m \quad (7)$$

where n_i is related to Q . The simulation result shown in Figure 2b indicates that R_{CSSR} increases with increasing N_S and Q (here the simulation parameters were $\text{TR}_{\text{DW}} = 13$ ms, $N_y = 48$, $N_b = 5$, $a = 1$, $\alpha_3 = 5.5^\circ$, $m = 24$ and $\tau = 2\text{--}400$ ms).

On the other hand, compared with the sequential 'DWI + CSSR' scheme, the diffusion measurement in DWCSSR is delayed. During the delay time, S_{gas} will be reduced as a result of both T_1 relaxation and gas exchange. For the centric phase-encoding DWI case, the SNR of DW images is proportional to S_{gas} during the first α_3 excitation. Thus, assuming that the first α_3 excitation is performed during the exchange time τ_{c+1} (i.e. $\tau_{c+1} \geq Q \cdot \text{TR}_{\text{DW}}$ and $\tau_c < Q \cdot \text{TR}_{\text{DW}}$), the ratio of SNR_{DWI} (SNR of DW images) in DWCSSR to that in the 'DWI + CSSR' scheme will be:

$$R_{\text{DWI}} = \exp\left[-\frac{\sum_{k=1}^c \tau_k + c \cdot \text{TR}_{\text{CSSR}}}{T_1}\right] \cdot \prod_{k=1}^c [1 - F(\tau_k)] \quad (8)$$

where TR_{CSSR} is the TR of CSSR (duration between two sequential excitations of α_1 when the exchange time is zero) and $\sum_{k=1}^c \tau_k + c \cdot \text{TR}_{\text{CSSR}}$ is the delay time.

According to Equations 7 and 8, various experimental parameters (such as N_S , Q and T_1) can affect the R_{CSSR} and R_{DWI} values. CSSR obtains NMR spectra, whereas DWI acquires two-dimensional images. Moreover, the total breath-hold time of DWCSSR is also affected by the experimental parameters, as shown in Figure 2c. Thus, it is hard to extract optimal parameters to preserve both SNR_{DWI} and SNR_{CSSR} . However, in order to preserve large R_{CSSR} values, an increase in N_S , as shown in Figure 2b, is beneficial. In addition, during certain N_S cases, a trade-off between SNR_{CSSR} and SNR_{DWI} can be realized by modulating the Q value. $R_{\text{CSSR}}(\tau_k)$ is proportional to Q , whereas R_{DWI} is inversely proportional to Q , as shown in Figure 2b and 2c. However, when considering that CSSR measures the average signals of the entire lung, whereas DWI measures signals of a single slice, it would be more rational to preserve a high SNR_{DWI} . Thus, in most cases, setting $Q = N_S$ will be beneficial.

3 | METHODS

3.1 | Experiments

In vivo studies were conducted on five Sprague–Dawley rats weighing 225 ± 26 g. Animal experiments were carried out in accordance with the guidelines provided and approved by the Institutional Review Board of Wuhan Institute of Physics and Mathematics (WIPM), Chinese Academy of Sciences (CAS). Rats were anesthetized with 5% isoflurane and maintained under 2.5% isoflurane. The animals were intubated with a 14G endotracheal tube tied to the trachea.

All the MR experiments were performed on a 7-T animal MRI scanner (Bruker BioSpec 70/20 USR, Germany) using a horizontal magnet equipped with a maximum gradient strength of 444.75 mT/m and Paravision 5.0 software. A home-built, eight-leg, rigid, transmit-receive birdcage coil (^{129}Xe at 83.072 MHz) was used, and connected to an RF amplifier with a maximum transmitter power of 625 W. A transmitter gain of -6.0 dB is roughly 625 W. If the transmitter gain increased by 6.02 dB, the transmitter power halved (e.g. 0.02 dB is roughly 312.5 W). Enriched xenon gas (86%) was polarized using a home-built, continuous-flow polarizer to a level of $\sim 20\%$. After thawing from frozen-collection, HP xenon gases were collected in a Tedlar bag, and successively passed into the lung using a home-built ventilator. Breathing sequences were the same as those described previously,²⁹ with a single xenon gas pre-wash.

DWCSSR, 'CSSR + DWI' and 'DWI + CSSR' were each repeated twice with and without slice selection during a single measurement, and six measurements were performed. For rat 1, DWI was operated without any diffusion-weighted gradient, phase-encoding gradient or read-out gradient, so as to observe the available gaseous ^{129}Xe magnetizations during each excitation. Both the flip angles and T_1 of ^{129}Xe gas in the lungs were calibrated by a single-breath method.²⁹ All RF pulses were based on a specially designed shape, as shown in Figure 3a.

The CSSR parameters were as follows: entire repetition number $m = 24$; $\text{TR}_{\text{CSSR}} = 17.8$ ms; exchange time τ varied from 2 to 400 ms²¹; all NMR spectra were acquired with a bandwidth of 29.76 kHz and 256 sampling points. α_1 and α_2 were centered at 204.5 ppm (by defining the gaseous ^{129}Xe signal as 0 ppm). The duration and transmitter gain of α_1 were 0.5 ms and -3.0 ± 0.4 dB, respectively, whereas those of α_2 were 0.43 ms and -4.3 ± 0.3 dB, respectively. The flip angles on the gaseous ^{129}Xe signal of both α_1 and α_2 were calculated by sequential on-resonance excitations of 204.5 ppm and 0 ppm. For different rats, the flip angles on the gaseous ^{129}Xe signal of α_1 were varied from 0.1° to 0.4° , and those of α_2 were varied from 0.9° to 1.4° . The excitation bandwidths of RF pulses α_1 and α_2 were equal to 14.04 and 16.33 kHz, respectively. Therefore, the RF pulses α_1 and α_2 can provide coordinated excitations of both dissolved ^{129}Xe signals in TP and RBCs.

In both the non-slice selection and multi-slice cases, the DWI parameters were as follows: matrix, 48×48 ; field of view, 6×6 cm²; gradient echoes were acquired with a bandwidth of 29.76 kHz; echo position, 30%; centric encoding; rise and fall time, 0.123 ms; constant time, 1.0 ms; diffusion time $\Delta = 1.3$ ms; under-sampling ratio $a = 1$. B values were derived from the integral of the gradient waveform as described previously.²⁸ α_3 was centered at 0 ppm. The duration and flip angle of α_3 were 0.5 ms and 5.5° , respectively. In the non-slice selection case, the DWI parameters were as follows: $\text{TR}_{\text{DW}} = 14.4$ ms; $\text{TE} = 3.4$ ms; ordinal b values, 0, 12, 24, 36 and 48 s/cm²; minimum DWI repetition number $Q = N_s$. In the multi-slice case, the DWI parameters were as follows: $\text{TR}_{\text{DW}}/\text{TE} = 15.3/4.2$ ms; ordinal b values, 0, 12 and 36 s/cm²; number of slices $N_s = 2$; slice thickness, 20 mm; $Q = N_s$. Figure 3b displays the sampling order of DW images in multi-slice DWCSR. The DWI repetitions of slice 1 to slice 2 with the same b value and phase encoding were performed during the same exchange times, in order to provide the same CSSR exchange conditions.

3.2 | Data analysis

All of the MR data were processed in MatLab (MathWorks, Natick, MA, USA).

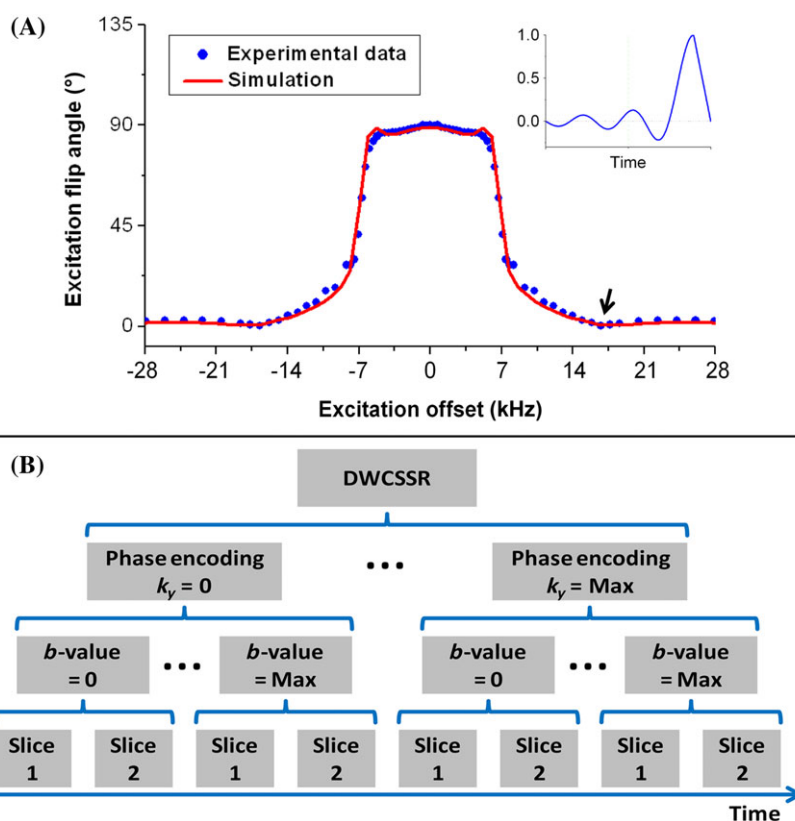


FIGURE 3 A, specially-designed shape of pulse used in experiments, which can provide nice slice selection property, as well as minimal on-resonance excitation of dissolved ^{129}Xe during the excitations of gaseous ^{129}Xe . Inset figure displays the time domain of this truncated-sinc shape pulse, which consists of 5 side lobes, a half central lobe and a linear drop. The black arrow in the frequency domain indicates the position of dissolved ^{129}Xe during the excitations of gaseous ^{129}Xe . B, sampling order of DWI during the multi-slices DWCSR case

NMR free induction decay (FIDs) were transformed to the complex Lorentzian by one-dimensional Fourier transform and phase correction. The integrals of the absorption Lorentzian were considered as the actual acquired signal intensities. Integral intervals were -6 ppm to 6 ppm for the gaseous signal, 220 ppm to 203 ppm for the RBC signal and 203 ppm to 180 ppm for the TP signal. When calculating $S_{\text{RBC}}/S_{\text{gas}}$ and $S_{\text{TP}}/S_{\text{gas}}$, the S_{gas} values were calculated using an average of the measurements from both the current and prior α_2 pulses to reduce the bias caused by the magnetization decay. Then, MOXE was fitted to CSSR data using a non-linear least-squares algorithm. The fitting equations and constant parameters were the same as those in Equations 1–5 and values described in a previous study,²¹ respectively. After fitting, the gas exchange function parameters of the lungs were acquired, including the fraction of RBC xenon in blood (η), the barrier-to-septum ratio (δ/d), the gas exchange time constant (T), the pulmonary capillary transit time (t_x), the septal wall thickness (d), the thickness of the air–blood barrier (δ), SVR and the blood hematocrit (Hct), etc.

For DWI data, echoes were rearranged into k spaces based on the sampling order shown in Figure 3b. Then, k -space data were transformed to images by two-dimensional Fourier transform. Pixel SNRs of magnitude images were calculated by $\text{SNR}(A) = I(A)/(\sigma_M/\sqrt{2-\pi/2})$,³⁰ where $I(A)$ is the intensity of pixel A and σ_M is the standard deviation of noise inside the corner of the magnitude image. After thresholding the image with $\text{SNR} > 3$, the mean SNR was calculated by averaging pixel SNRs inside the region of the entire lungs. A mean filtering operation was applied prior to further processing. All lung morphological parameters were obtained by fitting an anisotropic diffusion model to DW images, using a non-linear least-squares algorithm on a pixel-by-pixel basis. Fitting equations were the same as those (equations 2, 3, 5, 6 and 14) described previously.²⁸ The variable D_0 ³¹ of diluted ^{129}Xe in the lungs was in the range 0.059 – 0.14 cm^2/s .²⁴ In each image, pixels of $\text{SNR} < 3$ were removed during fitting, because $\text{SNR} = 3$ has been suggested as a minimum SNR in DWI analysis.³²

4 | RESULTS

Figure 4 displays the measured gaseous ^{129}Xe signals during the corresponding ‘CSSR + DWI’, ‘DWI + CSSR’ and DWCSSR schemes. In the non-slice selection case, both the ‘CSSR + DWI’ and ‘DWI + CSSR’ schemes required a breath-hold time of approximately 6.3 s, whereas DWCSSR only required a breath-hold time of approximately 4 s. The total acquisition time was reduced by 35% . Meanwhile, the gaseous ^{129}Xe signals of both DWI and CSSR by the DWCSSR scheme were relatively high compared with those of the other two schemes. The CSSR signals by the ‘DWI + CSSR’ scheme were only $\sim 25\%$ of those by DWCSSR. In the multi-slice case, which is not shown in the figure, both the breath-hold time shortening (reduced from 7.2 to 5.2 s by DWCSSR) and high gaseous ^{129}Xe signals were seen.

The representative dynamics of dissolved ^{129}Xe and gaseous ^{129}Xe signals during CSSR acquisitions are shown in Figure 5a–c. Quantitative S_{RBC} , S_{TP} and S_{gas} values are shown in Figure 5b–f, respectively. The amplitudes of both dissolved ^{129}Xe and gaseous ^{129}Xe signals in DWCSSR schemes are smaller than those in the ‘CSSR + DWI’ scheme during long exchange times, owing to the extra RF excitations of gaseous ^{129}Xe . However, during short exchange times, the signals in DWCSSR are the same as those in ‘CSSR + DWI’. These measured S_{RBC} , S_{TP} and S_{gas} values fit very well with the predicted values, which were calculated according to Equation 7. Figure 5g displays the decays of S_{gas} values within the 400 ms exchange time, which were calculated by dividing the current $S_{\text{gas}}(t_k)$ values by the

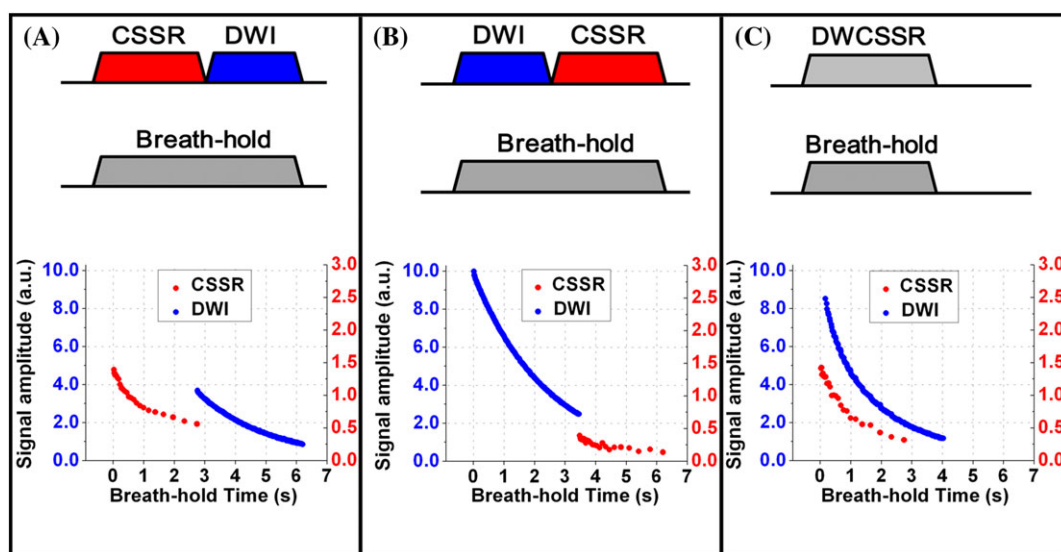


FIGURE 4 Diagrams of the sequential ‘CSSR + DWI’ scheme A, sequential ‘DWI + CSSR’ scheme B and diffusion-weighted chemical shift saturation recovery (DWCSSR) scheme C, and the corresponding measured gaseous ^{129}Xe signals of chemical shift saturation recovery (CSSR) (red) and diffusion-weighted imaging (DWI) (blue). Here, the gaseous ^{129}Xe signals were acquired without any diffusion-weighted gradient, phase-encoding gradient or read-out gradient. It should be noted that the total breath-hold time needed for DWCSSR is shortened from 6.3 to 4 s, and the gaseous ^{129}Xe signals of both CSSR and DWI are relatively higher in DWCSSR

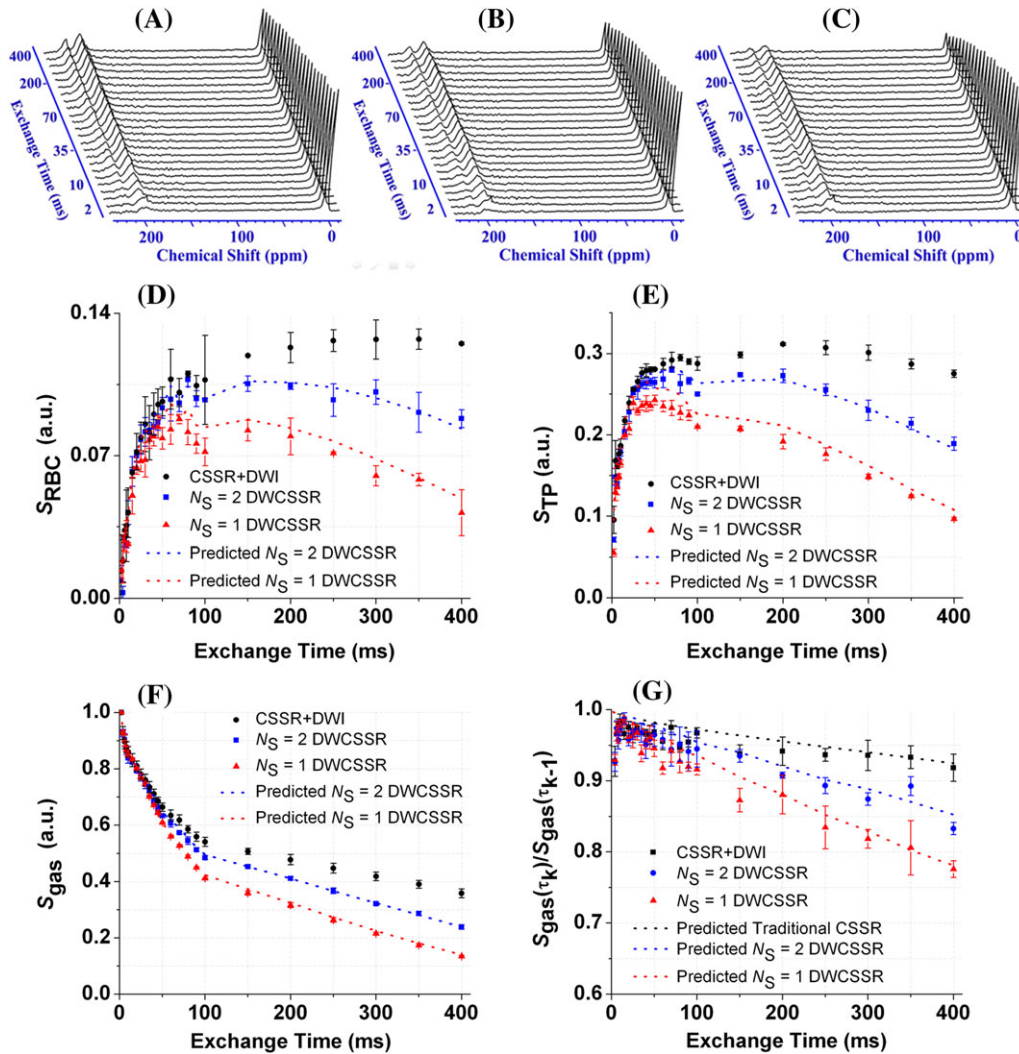


FIGURE 5 Representative dynamics of the dissolved ^{129}Xe and gaseous ^{129}Xe signals during chemical shift saturation recovery (CSSR) acquisitions by 'CSSR + DWI' A, multi-slice ($N_S = 2$) diffusion-weighted chemical shift saturation recovery (DWCSSR) B and non-slice selection ($N_S = 1$) DWCSSR C. D–G quantitative S_{RBC} , S_{TP} , S_{gas} and $S_{gas}(\tau_k)/S_{gas}(\tau_{k-1})$ values (points and error bars) and the corresponding theoretical predicted values (dotted lines). It should be noted that the measured values fit well with the predicted values. Points and error bars represent mean values and standard deviations in six measurements, respectively. DWI, diffusion-weighted imaging; RBC, red blood cell; TP, tissue and plasma

prior $S_{gas}(\tau_{k-1})$ values. The maximum losses of S_{gas} within the 400 ms exchange time are around 23%, 17% and 8% for non-slice selection ($N_S = 1$) DWCSSR, multi-slice ($N_S = 2$) DWCSSR and 'CSSR + DWI' cases, respectively. Decays of S_{gas} values also fit well with the predicted values, which were calculated according to Equation 6. Among Figure 5b–g, the decay rates of signals during $N_S = 2$ DWCSSR are significantly slower than those during $N_S = 1$ DWCSSR.

CSSR build-up curves of the DWCSSR scheme are slightly smaller than those of the 'CSSR + DWI' scheme, in both the non-slice selection and multi-slice case, as shown in Figure 6a and 6b, respectively. However, the gas exchange function parameters of DWCSSR are very close to those of 'CSSR + DWI' among all three representative rats, as shown in Figure 6c–e.

Figure 7 displays representative SNR maps of $b = 0$ DW images during 'CSSR + DWI', 'DWI + CSSR' and DWCSSR schemes. The $b = 0$ DW images of the DWCSSR scheme maintain a high SNR in comparison with those of 'CSSR + DWI' and 'DWI + CSSR' schemes, in both the non-slice selection case and multi-slice case. In the non-slice selection case, the quantitative SNR (15.5 ± 10.5) of the $b = 0$ DW image by the DWCSSR scheme shows a 125% increase compared with that (6.9 ± 4.7) of the 'CSSR + DWI' scheme, and is only 20% lower than that (18.7 ± 13.8) of the 'DWI + CSSR' scheme. Meanwhile, in the multi-slice case, SNR maps of the DWCSSR scheme are also comparable with those of the 'DWI + CSSR' scheme in both slices.

Figure 8 shows representative lung morphometry and diffusion coefficient maps obtained by non-slice selection DWI experimental data, where the D_L and D_T values are based on $b = 48 \text{ s/cm}^2$. Quantitative mean values of these parameters are displayed in Figure 9. Among the displayed results of two representative rats, the R , r and D_T values of the DWCSSR scheme are very close to those of the 'DWI + CSSR' scheme, whereas the L_m , D_L and D_0 values of the DWCSSR scheme are slightly increased. The 'CSSR + DWI' results are also close to those of the 'DWI + CSSR' scheme. However, as shown in Figure 8, the pixel numbers of the lung morphometry maps by the 'CSSR + DWI'

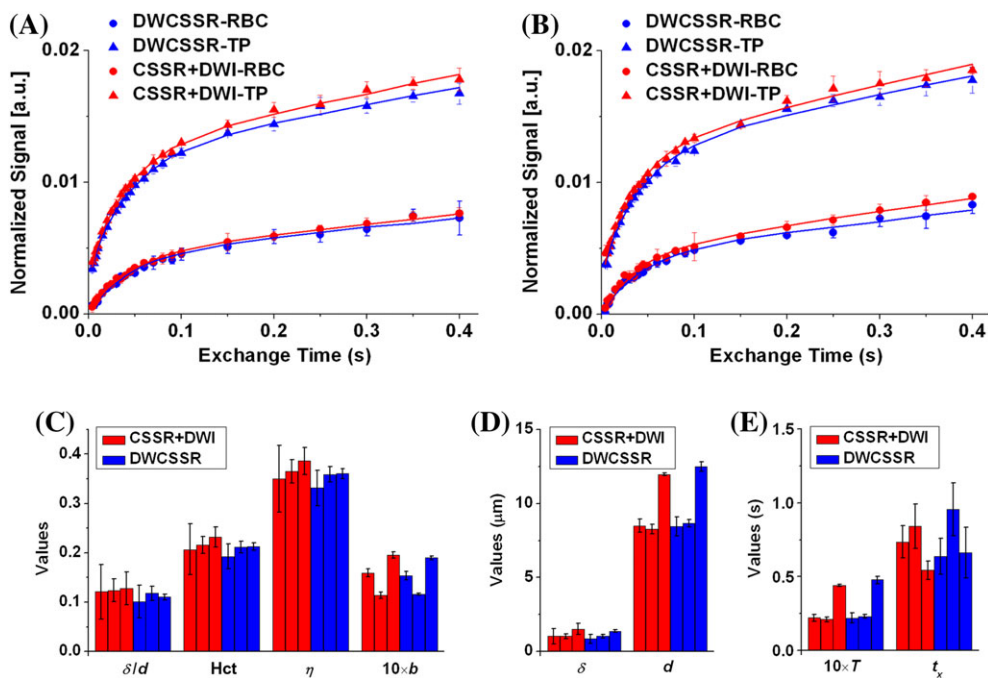


FIGURE 6 Representative chemical shift saturation recovery (CSSR) build-up curves in the non-slice selection case A and multi-slice case B. Full lines represent fitted curves of the model of xenon exchange (MOXE). C–E, gas exchange functional parameters of the lungs obtained by fitting MOXE to the corresponding CSSR data in three representative rats. For each parameter, the three bars of one color show the corresponding values of rats 1, 2 and 3 from left to right, respectively. It should be noted that the parameters measured by diffusion-weighted chemical shift saturation recovery (DWCSSR) are very close to those measured by 'CSSR + DWI'. DWI, diffusion-weighted imaging; Hct, hematocrit; RBC, red blood cell; TP, tissue and plasma

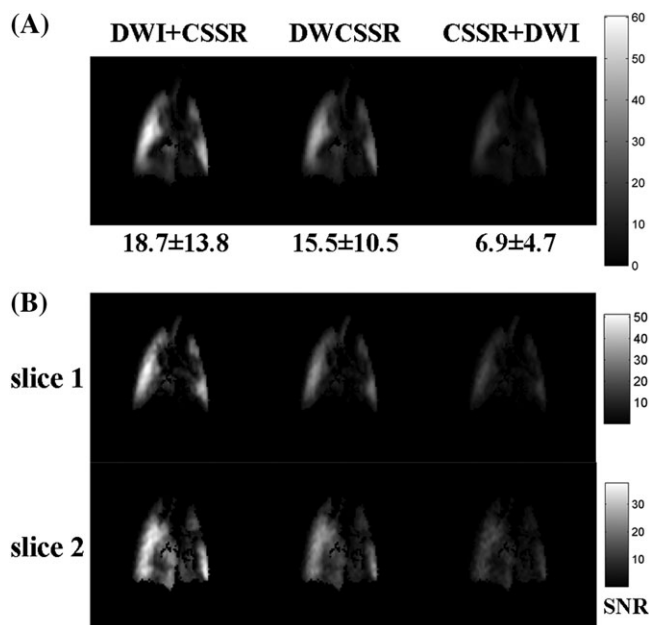


FIGURE 7 Signal-to-noise ratio (SNR) maps of $b = 0$ diffusion-weighted (DW) images in the non-slice selection case A, and multi-slice case B. Quantitative values of mean SNR and standard deviation are shown below the corresponding maps in A. Maps were averaged from six measurements and zero-filled to 96×96 . CSSR, chemical shift saturation recovery; DWI, diffusion-weighted imaging; DWCSSR, diffusion-weighted chemical shift saturation recovery

scheme are significantly reduced compared with those of the other two schemes. Thus, the DWI results of the 'CSSR + DWI' scheme cannot indicate the actual values of the whole lungs. In comparison, the lung morphometry and diffusion coefficient maps of the DWCSSR scheme are quite similar to those of the 'DWI + CSSR' scheme.

Table 1 shows the measured SVR values of all rats. The SVR measured by DWI ($\sim 400 \text{ cm}^{-1}$) is approximately 2.5-fold that measured by CSSR ($\sim 160 \text{ cm}^{-1}$). Moreover, the results for the DWCSSR scheme are close to those of the sequential schemes, among all rats.

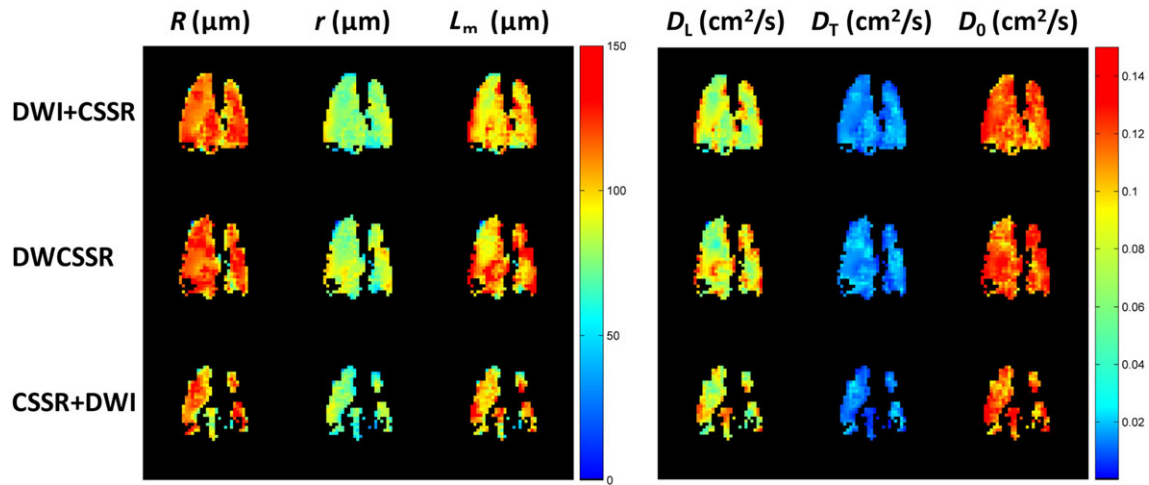


FIGURE 8 Representative lung morphological maps (R , r , L_m) and diffusion coefficient maps (D_L , D_T , D_0) based on non-linear fitting of non-slice selection multiple b -value diffusion-weighted imaging (DWI). It should be noted that the maps of the diffusion-weighted chemical shift saturation recovery (DWCSSR) scheme are similar to those of the 'DWI + CSSR' scheme. CSSR, chemical shift saturation recovery

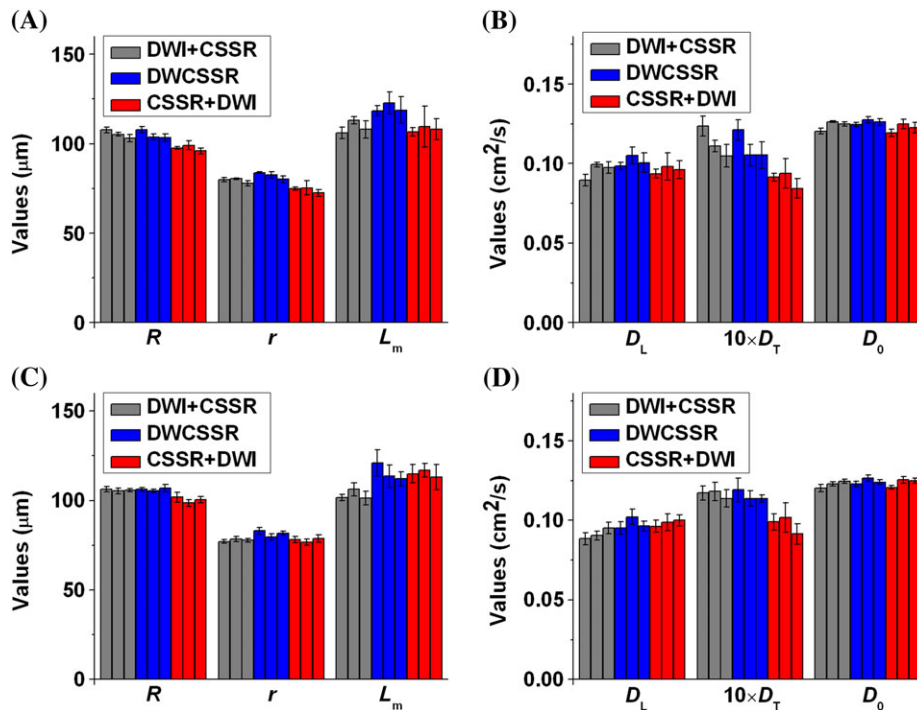


FIGURE 9 Representative gas diffusion function parameters of rat 2 A,B and rat 3 C,D. For each parameter, the three bars of one color show the corresponding values of the non-slice selection case, slice 1 and slice 2 from left to right, respectively. It should be noted that the values of the diffusion-weighted chemical shift saturation recovery (DWCSSR) scheme are close to those of the 'DWI + CSSR' scheme. CSSR, chemical shift saturation recovery; DWI, diffusion-weighted imaging

TABLE 1 Comparison of the calculated surface-to-volume ratios (SVRs) (cm^{-1}) by CSSR and DWI^a

		Rat 1	Rat 2	Rat 3	Rat 4	Rat 5
CSSR	CSSR + DWI	177.6 ± 5.7	137.8 ± 6.0	163.0 ± 4.0	184.8 ± 2.4	159.4 ± 7.5
	DWCSSR	172.0 ± 7.2	134.1 ± 2.8	151.9 ± 0.8	183.2 ± 3.2	154.9 ± 9.9
DWI	CSSR + DWI	-	399.8 ± 19.1	416.9 ± 9.6	481.2 ± 23.9	396.7 ± 17.6
	DWCSSR	-	388.6 ± 9.5	370.4 ± 4.4	423.5 ± 15.6	395.6 ± 21.1
	DWI + CSSR	-	421.9 ± 9.8	400.9 ± 9.8	448.2 ± 13.8	423.8 ± 11.2

CSSR, chemical shift saturation recovery; DWI, diffusion-weighted imaging; DWCSSR, diffusion-weighted chemical shift saturation recovery.

^aDWI results of rat 1 are not shown because the acquisition data for rat 1 are nuclear magnetic resonance (NMR) spectra.

5 | DISCUSSION

The clinical application of HP gas MRI needs to consider its practicability, cost and efficiency. Compared with ^3He MRI, ^{129}Xe MRI has a lower cost. However, most of the ^{129}Xe MR techniques are performed during different breath-holds. Only a few studies,^{13,15,33,34} have focused on accelerating sampling during shorter single breath-holds. CSSR and DWI are both powerful techniques in pulmonary function detection, and have been applied to various pulmonary disease studies. The DWCSSR method proposed in this study, combining these two techniques, accelerates the acquisition of both DWI and CSSR data. Two advantages of the DWCSSR method, i.e. reducing the breath-hold time whilst maintaining high SNR for both DWI and CSSR data, make it efficient and practical. Our experimental results indicate that the sequential single breath-hold schemes are both suboptimal compared with DWCSSR.

Moreover, after the acquisition of DWI and CSSR data, various pulmonary function parameters can be obtained. In this study, we fitted MOXE to CSSR data, and the Weibel model to DWI data. Thus, both gas exchange function parameters and gas diffusion function parameters were obtained. Indeed, CSSR data could also be combined with the Patz model and Månsson model, whereas the DWI data could be combined with the diffusional kurtosis imaging (DKI) model³⁵ or stretched exponential model.³⁶ In general, the DWCSSR method can be combined with various post-processing paths.

The essence of this study is the performance of other techniques during the exchange times of CSSR. In theory, in addition to the DWI sequence, a two- or three-dimensional spoiled gradient echo sequence can also be performed during the exchange times of CSSR, so that both ventilation maps of lung and CSSR data can be acquired within a shortened breath-hold. This study proposes this accelerating idea and verifies its feasibility. Further acquisition schemes can be proposed based on this idea.

However, influences on DWI and CSSR data should be discussed during the DWCSSR scheme. In the theoretical part, we speculate that the SNRs and decay rate of gaseous ^{129}Xe longitudinal magnetization during DWCSSR could be slowed down by increasing the number of slices N_s . This is supported by the experimental results in Figure 5. The well-fitted curves between the measured CSSR signals and the predicted values in Figure 5 also verify the validity of Equations 6 and 7. In both the non-slice selection and multi-slice cases, the measured CSSR build-up curves and gas exchange functional parameters (Figure 6) of DWCSSR are quite close to those of traditional CSSR. As MOXE is robust against moderate noise,¹⁹ the almost 50% reduced SNR during the long exchange times of DWCSSR (see Figure 2b) would not have a significant influence on the measurement of gas exchange. These results also indicate that it is important to normalize the dissolved ^{129}Xe signals. Moreover, we applied a specially designed chemical shift selected pulse in order to gain minimal on-resonance excitation of dissolved ^{129}Xe during the excitation of α_3 . The flip angle of on-resonance excitation of dissolved ^{129}Xe was only $\sim 0.02^\circ$, whereas $\alpha_3 = 5.5^\circ$. This slight excitation of dissolved ^{129}Xe can be neglected. Meanwhile, DWI repetitions of different slices were performed during the same exchange times, and the slice distance of DW images was zero. Thus, the excitations of gaseous ^{129}Xe during the exchange times can be considered as homogeneous. Therefore, in our experimental results, CSSR data of DWCSSR remain quite close to those in the traditional CSSR sequence in both the non-slice selection and multi-slice cases.

DWI data are commonly affected by the decay of the gaseous ^{129}Xe signal, which is related to both T_1 and the flip angles on the gaseous ^{129}Xe signal of the RF pulses α_1 , α_2 and α_3 . In addition, following each saturation of dissolved ^{129}Xe (i.e. RF pulse α_1), there is an extra decay of the gaseous ^{129}Xe signal related to the gas exchange. In our experiments, the flip angles on the gaseous ^{129}Xe signal of RF pulses α_1 and α_2 were small (0.1° – 0.3° for RF pulse α_1 , and 0.8° – 1.1° for RF pulse α_2), and the total excitation numbers of RF pulses α_1 and α_2 were only 24. Thus, the excitations on the gaseous ^{129}Xe signal of RF pulses α_1 and α_2 can be ignored. The excitations of the RF pulse α_3 and longitudinal relaxation also exist in the traditional DWI scheme. Therefore, compared with the traditional DWI scheme, the maximal influence on DWI data of the DWCSSR scheme is the decay of the gaseous ^{129}Xe signal related to gas exchange. This effect can explain the slight increased diffusion parameter values of the DWCSSR scheme in Figure 9. In order to avoid this effect on DWI data, further studies can be focused on the variable flip angle (VFA) scheme,³⁷ for which it is possible to yield constant signal during DWI excitations of DWCSSR.

In addition, there are three limitations of the DWCSSR method. The first is the need for both good slice selection and excellent selective excitation properties of the RF pulse. In this study, as a result of the susceptibility difference between the alveolar gas and the pulmonary tissue in the lungs, T_2^* of the ^{129}Xe signals at 7 T is quite short ($T_2^* < 3$ ms). Thus, in order to improve SNR, we applied a truncated sinc-shaped pulse. However, for human studies, T_2^* of ^{129}Xe signals can be longer,³⁸ so that a relatively complete sinc-shaped pulse or binomial composite pulse³⁹ can be applied. The second limitation is that the slice distance should be equal to zero in the multi-slice case, in order to keep the same exchange conditions for different slices in CSSR. Thus, cross-slice excitations cannot be applied in the DWCSSR sequence. The third limitation is the impact of B_1 inhomogeneity of the coil, which might affect the actual value of the flip angle. However, this can be improved by using more homogeneous transmitter coils, such as a birdcage coil. In this study, the B_1 inhomogeneity of the birdcage coil is about 4.6%, which can yield a comparable uniform excitation.

Although the experiments in this study were performed on small animals, DWCSSR can also be applied to human studies. In simulations, when setting the CSSR and DWI parameters to those in conventional human studies^{40–42} (such as $\text{TR}_{\text{CSSR}} = 30$ ms, $m = 36$, $\tau = 4$ – 900 ms, $\text{TR}_{\text{DW}} = 13$ ms, $N_b = 6$, $N_y = 40$, $N_s = 4$, $T_1 = 15$ s, $Q = N_s$, $a = 1$; gas exchange function parameters the same as in Chang¹⁹; flip angles the same as the values in our experiments), DWCSSR can shorten the breath-hold time from ~ 20 s to ~ 14.5 s compared with 'CSSR + DWI' and 'DWI + CSSR' schemes. Meanwhile, the DWI signals of DWCSSR can be increased by close to 100% compared with those of the 'CSSR + DWI' scheme, whereas the CSSR data remain the same. However, application of the DWCSSR method to human studies should consider the specific absorption ratio (SAR), which depends on different coils.

It is interesting that the SVR values obtained from the CSSR method ($\sim 160 \text{ cm}^{-1}$) are much smaller than those from DWI ($\sim 400 \text{ cm}^{-1}$). In comparison with the SVR values of 698 cm^{-1} in mice³ and of 200 cm^{-1} in humans⁴³ by DWI, it is reasonable that the SVR values by DWI in rats from this study fall in between. However, DWI is image based, whereas CSSR is single voxel based without spatial resolution. Thus, the calculated SVR in CSSR probably includes regions of the lung with little gas exchange, such as in the upper airways including the trachea, where SVR is a lot lower. Moreover, in MOXE, tissue is assumed to be sandwiched between airspaces. In reality, there is blood next to the boundaries of the lung that only sees airspace on one side. Thus, SVR in such boundary region would also be lower (approximately halved). In comparison with CSSR, the morphometry method has no such problems because the calculations are based on diffusion inside the airspaces. Moreover, in CSSR, SVR is calculated by $\text{SVR} = \frac{2b}{\lambda d}$. Thus, the calculation of SVR is strongly dependent on the scaling factor b . In this study, we regard the integrals of the absorption Lorentzian as the acquired signal intensities, so that scaling factor b values are ~ 0.015 (see Figure 6c). However, if we regard the peak amplitudes as the acquired signal intensities, the scaling factor b values would be ~ 0.005 , and result in smaller SVR values ($\sim 53 \text{ cm}^{-1}$), which are close to the rat results obtained previously.²¹ In Stewart et al.,⁴ the signal intensities were calculated by integration of the respective NMR peaks in the magnitude spectra. In this way, the calculated SVR values are $\sim 110 \text{ cm}^{-1}$ in our study. Thus, the accurate calculation of SVR values by CSSR is somewhat challenging. Fortunately, the measurement of other gas exchange parameters in CSSR is not affected by the calibration of the scaling factor b .

6 | CONCLUSIONS

We propose a new method, referred to as DWCSSR, to perform ^{129}Xe DWI and CSSR within a single breath-hold. The essence of DWCSSR is to perform DWI repetitions within the exchange times of CSSR. DWCSSR is able to shorten the total breath-hold time when fulfilling both CSSR and DWI within a single breath-hold. Meanwhile, high SNR of both CSSR and DWI data can be gained by DWCSSR. We compared DWCSSR with sequential single breath-hold schemes (i.e. 'CSSR + DWI' and 'DWI + CSSR' schemes). The results indicate that DWCSSR is practical and efficient. Coupled with lung models, such as MOXE and the Weibel model, DWCSSR is able to obtain accurate parameters related to lung morphometry and gas exchange function. The good practicability of the DWCSSR method indicates that it has great potential for the evaluation and diagnosis of pulmonary diseases.

ACKNOWLEDGEMENTS

This work was funded by the National Natural Science Foundation of China (81227902, 81625011), National Program for Support of Eminent Professionals (National Program for Support of Top-notch Young Professionals) and the Opening Project of Wuhan National High Magnetic Field Center (Grant No.2015KF09), Huazhong University of Science and Technology. The authors thank Dr Qiuchen Rao and Dr Ming Zhang for help with animal experiments.

REFERENCES

1. Yablonskiy DA, Sukstanskii AL, Leawoods JC, et al. Quantitative in vivo assessment of lung microstructure at the alveolar level with hyperpolarized ^3He diffusion MRI. *Proc Natl Acad Sci U S A*. 2002;99(5):3111-3116.
2. Altes TA, Powers PL, Knight-Scott J, et al. Hyperpolarized He-3 MR lung ventilation imaging in asthmatics: Preliminary findings. *J Magn Reson Imaging*. 2001;13(3):378-384.
3. Wang W, Nguyen NM, Yablonskiy DA, et al. Imaging lung microstructure in mice with hyperpolarized He-3 diffusion MRI. *Magn Reson Med*. 2011;65(3):620-626.
4. Stewart NJ, Leung G, Norquay G, et al. Experimental validation of the hyperpolarized Xe-129 chemical shift saturation recovery technique in healthy volunteers and subjects with interstitial lung disease. *Magn Reson Med*. 2015;74(1):196-207.
5. Mugler JP, Altes TA, Ruset IC, et al. Simultaneous magnetic resonance imaging of ventilation distribution and gas uptake in the human lung using hyperpolarized xenon-129. *Proc Natl Acad Sci U S A*. 2010;107(50):21 707-21 712.
6. Driehuys B, Cofer GP, Pollaro J, Mackel JB, Hedlund LW, Johnson GA. Imaging alveolar-capillary gas transfer using hyperpolarized Xe-129 MRI. *Proc Natl Acad Sci U S A*. 2006;103(48):18 278-18 283.
7. Ruset IC, Ketel S, Hersman FW. Optical pumping system design for large production of hyperpolarized Xe-129. *Phys Rev Lett*. 2006;96(5):053002.
8. Norquay G, Parnell SR, Xu X, Parra-Robles J, Wild JM. Optimized production of hyperpolarized Xe-129 at 2 bars for in vivo lung magnetic resonance imaging. *J Appl Phys*. 2013;113(4):044908.
9. Nikolaou P, Coffey AM, Walkup LL, et al. Near-unity nuclear polarization with an open-source Xe-129 hyperpolarizer for NMR and MRI. *Proc Natl Acad Sci U S A*. 2013;110(35):14 150-14 155.
10. Mugler JP, Altes TA. Hyperpolarized ^{129}Xe MRI of the human lung. *J Magn Reson Imaging*. 2013;37(2):313-331.
11. Mugler JP, Driehuys B, Brookeman JR, et al. MR imaging and spectroscopy using hyperpolarized Xe-129 gas: Preliminary human results. *Magn Reson Med*. 1997;37(6):809-815.
12. Qing K, Ruppert K, Jiang Y, et al. Regional mapping of gas uptake by blood and tissue in the human lung using hyperpolarized xenon-129 MRI. *J Magn Reson Imaging*. 2014;39(2):346-359.
13. Kaushik SS, Robertson SH, Freeman MS, et al. Single-breath clinical imaging of hyperpolarized Xe-129 in the airspaces, barrier, and red blood cells using an interleaved 3D radial 1-point Dixon acquisition. *Magn Reson Med*. 2016;75(4):1434-1443.

14. Ruppert K, Brookeman JR, Hagspiel KD, Mugler JP. Probing lung physiology with xenon polarization transfer contrast (XTC). *Magn Reson Med*. 2000;44(3):349-357.
15. Muradyan I, Butler JP, Dabaghyan M, et al. Single-breath xenon polarization transfer contrast (SB-XTC): Implementation and initial results in healthy humans. *J Magn Reson Imaging*. 2013;37(2):457-470.
16. Månsson S, Wolber J, Driehuys B, Wollmer P, Golman K. Characterization of diffusing capacity and perfusion of the rat lung in a lipopolysaccharide disease model using hyperpolarized Xe-129. *Magn Reson Med*. 2003;50(6):1170-1179.
17. Butler JP, Mair RW, Hoffmann D, et al. Measuring surface-area-to-volume ratios in soft porous materials using laser-polarized xenon interphase exchange nuclear magnetic resonance. *J Phys-Condens Mater*. 2002;14(13):L297-L304.
18. Patz S, Muradyan I, Hrovat MI, et al. Diffusion of hyperpolarized Xe-129 in the lung: A simplified model of Xe-129 septal uptake and experimental results. *New J Phys*. 2011;13(1):015009.
19. Chang YV. MOXE: A model of gas exchange for hyperpolarized ^{129}Xe magnetic resonance of the lung. *Magn Reson Med*. 2013;69(3):884-890.
20. Qing K, Mugler JP, Altes TA, et al. Assessment of lung function in asthma and COPD using hyperpolarized ^{129}Xe chemical shift saturation recovery spectroscopy and dissolved-phase MRI. *NMR Biomed*. 2014;27(12):1490-1501.
21. Li H, Zhang Z, Zhao X, Sun X, Ye C, Zhou X. Quantitative evaluation of radiation-induced lung injury with hyperpolarized xenon magnetic resonance. *Magn Reson Med*. 2016;76(2):408-416.
22. Santyr G, Fox M, Thind K, et al. Anatomical, functional and metabolic imaging of radiation-induced lung injury using hyperpolarized MRI. *NMR Biomed*. 2014;27(12):1515-1524.
23. Ouriadov A, Farag A, Kirby M, McCormack DG, Parraga G, Santyr GE. Lung morphometry using hyperpolarized Xe-129 apparent diffusion coefficient anisotropy in chronic obstructive pulmonary disease. *Magn Reson Med*. 2013;70(6):1699-1706.
24. Ouriadov A, Farag A, Kirby M, McCormack DG, Parraga G, Santyr GE. Pulmonary hyperpolarized Xe-129 morphometry for mapping xenon gas concentrations and alveolar oxygen partial pressure: Proof-of-concept demonstration in healthy and COPD subjects. *Magn Reson Med*. 2015;74(6):1726-1732.
25. Mata JF, Altes TA, Cai J, et al. Evaluation of emphysema severity and progression in a rabbit model: Comparison of hyperpolarized He-3 and Xe-129 diffusion MRI with lung morphometry. *J Appl Physiol*. 2007;102(3):1273-1280.
26. Boudreau M, Xu X, Santyr GE. Measurement of ^{129}Xe gas apparent diffusion coefficient anisotropy in an elastase-instilled rat model of emphysema. *Magn Reson Med*. 2013;69(1):211-220.
27. Kaushik SS, Cleveland ZI, Cofer GP, et al. Diffusion-weighted hyperpolarized ^{129}Xe MRI in healthy volunteers and subjects with chronic obstructive pulmonary disease. *Magn Reson Med*. 2011;65(4):1155-1165.
28. Sukstanskii AL, Yablonskiy DA. Lung morphometry with hyperpolarized ^{129}Xe : Theoretical background. *Magn Reson Med*. 2012;67(3):856-866.
29. Zhong JP, Ruan WW, Han YQ, Sun XP, Ye CH, Zhou X. Fast determination of flip angle and T-1 in hyperpolarized gas MRI during a single breath-hold. *Sci Rep*. 2016;6:25 854.
30. Gudbjartsson H, Patz S. The rician distribution of noisy MRI data. *Magn Reson Med*. 1995;34(6):910-914.
31. Ouriadov A, Fox M, Hegarty E, Parraga G, Wong E, Santyr GE. Early stage radiation-induced lung injury detected using hyperpolarized Xe-129 morphometry: Proof-of-concept demonstration in a rat model. *Magn Reson Med*. 2016;75(6):2421-2431.
32. Jones DK, Knosche TR, Turner R. White matter integrity, fiber count, and other fallacies: The do's and don'ts of diffusion MRI. *Neuroimage*. 2013;73:239-254.
33. Abdeen N, Cross A, Cron G, et al. Measurement of xenon diffusing capacity in the rat lung by hyperpolarized ^{129}Xe MRI and dynamic spectroscopy in a single breath-hold. *Magn Reson Med*. 2006;56(2):255-264.
34. Rao M, Wild JM. RF instrumentation for same-breath triple nuclear lung MR imaging of H-1 and hyperpolarized ^3He and Xe-129 at 1.5T. *Magn Reson Med*. 2016;75(4):1841-1848.
35. Trampel R, Jensen JH, Lee RF, Kamenetskiy I, McGuinness G, Johnson G. Diffusional kurtosis imaging in the lung using hyperpolarized ^3He . *Magn Reson Med*. 2006;56(4):733-737.
36. Chan HF, Stewart NJ, Parra-Robles J, Collier GJ, Wild JM. Whole lung morphometry with 3D multiple b-value hyperpolarized gas MRI and compressed sensing. *Magn Reson Med*. 2016; <https://doi.org/10.1002/mrm.26279>.
37. Zhao L, Mulkern R, Tseng CH, et al. Gradient-echo imaging considerations for hyperpolarized Xe-129 MR. *J Magn Reson Ser B*. 1996;113(2):179-183.
38. Xu X, Norquay G, Parnell SR, et al. Hyperpolarized Xe-129 gas lung MRI-SNR and T_2^* comparisons at 1.5 T and 3 T. *Magn Reson Med*. 2012;68(6):1900-1904.
39. Leung G, Norquay G, Schulte RF, Wild JM. Radiofrequency pulse design for the selective excitation of dissolved Xe-129. *Magn Reson Med*. 2015;73(1):21-30.
40. Chang YV, Quirk JD, Ruset IC, Atkinson JJ, Hersman FW, Woods JC. Quantification of human lung structure and physiology using hyperpolarized Xe-129. *Magn Reson Med*. 2014;71(1):339-344.
41. Quirk JD, Sukstanskii AL, Woods JC, et al. Experimental evidence of age-related adaptive changes in human acinar airways. *J Appl Physiol*. 2016;120(2):159-165.
42. Chang YV, Quirk JD, Yablonskiy DA. In vivo lung morphometry with accelerated hyperpolarized He-3 diffusion MRI: A preliminary study. *Magn Reson Med*. 2015;73(4):1609-1614.
43. Woods JC, Choong CK, Yablonskiy DA, et al. Hyperpolarized He-3 diffusion MRI and histology in pulmonary emphysema. *Magn Reson Med*. 2006;56(6):1293-1300.